

Uncovering multiple Wolf-Rayet star-clusters and the ionized ISM in Mrk 178: the closest metal-poor Wolf-Rayet HII galaxy

C. Kehrig^{1*}, E. Pérez-Montero¹, J.M. Vílchez¹, J. Brinchmann², D. Kunth³,
R. García-Benito¹, P. A. Crowther⁴, J. Hernández-Fernández⁵, F. Durret³, T. Contini^{6,7},
A. Fernández-Martín¹ and B.L. James⁸

¹*Instituto de Astrofísica de Andalucía, CSIC, Apartado de correos 3004, 18080 Granada, Spain*

²*Leiden Observatory, Leiden University, PO Box 9513, 2300 RA Leiden, The Netherlands*

³*Institut d'Astrophysique de Paris, UMR 7095 CNRS, Université Pierre & Marie Curie, 98 bis boulevard Arago, 75014 Paris, France*

⁴*Department of Physics & Astronomy, University of Sheffield, Hicks Building, Hounsfield Road, Sheffield S3 7RH, United Kingdom*

⁵*Departamento de Astronomia, Instituto de Astronomia, Geofísica e Ciências Atmosféricas da USP, Rua do Matão 1226, Cidade Universitária 05508-090 São Paulo, Brazil*

⁶*Institut de Recherche en Astrophysique et Planétologie (IRAP), CNRS, 14 avenue Édouard Belin, F-31400 Toulouse, France*

⁷*IRAP, Université de Toulouse, UPS-OMP, Toulouse, France*

⁸*Institute of Astronomy, University of Cambridge, Madingley Road, Cambridge, CB3 0HA, United Kingdom*

Accepted Date. Received Date; in original Date

ABSTRACT

New integral field spectroscopy (IFS) has been obtained for the nearby metal-poor Wolf-Rayet (WR) galaxy Mrk 178 to examine the spatial correlation between its WR stars and the neighbouring ionized interstellar medium (ISM). The strength of the broad WR features and its low metallicity make Mrk 178 an intriguing object. We have detected the blue and red WR bumps in different locations across the field-of-view ($\sim 300 \text{ pc} \times 230 \text{ pc}$) in Mrk 178. The study of the WR content has been extended, for the first time, beyond its brightest star-forming knot uncovering new WR star-clusters. Using SMC/LMC-template WR stars we empirically estimate a minimum of ~ 20 WR stars within the region sampled. Maps of the spatial distribution of the emission-lines and of the physical-chemical properties of the ionized ISM have been created and analyzed. Here we refine the statistical methodology by Pérez-Montero et al. (2011) to probe the presence of variations in the ISM properties. An error-weighted mean of $12+\log(\text{O}/\text{H})=7.72 \pm 0.01$ is taken as the representative oxygen abundance for Mrk 178. A localized N and He enrichment, spatially correlated with WR stars, is suggested by this analysis. Nebular $\text{HeII}\lambda 4686$ emission is shown to be spatially extended reaching well beyond the location of the WR stars. This spatial offset between WRs and HeII emission can be explained based on the mechanical energy input into the ISM by the WR star winds, and does not rule out WR stars as the HeII ionisation source. We study systematic aperture effects on the detection and measurement of the WR features, using SDSS spectra combined with the power of IFS. In this regard, the importance of targeting low metallicity nearby systems is discussed.

Key words: galaxies: dwarf — galaxies: individual: Mrk 178 — galaxies: ISM — galaxies: abundances — stars: Wolf-Rayet

1 INTRODUCTION

HII galaxies are local, gas-rich, systems with observable properties dominated by young and massive star clusters (e.g., Melnick, Terlevich, & Eggleton 1985; Campos-Aguilar, Moles, & Masegosa 1993; Popescu & Hopp 2000; Kehrig, Telles, & Cuisinier 2004; Westera et al. 2004). HII galaxies are also low metallicity objects [$7.0 \leq 12+\log(\text{O}/\text{H}) \leq 8.3$] in comparison with the solar metallicity [$12+\log(\text{O}/\text{H})_{\odot}=8.69$;

Asplund et al. (2009)], and actually include the most metal poor systems known in the local universe (e.g., Kehrig et al. 2006; Westera et al. 2012), for instance IZw18 with $12+\log(\text{O}/\text{H}) \approx 7.2$ (e.g., Vílchez & Iglesias-Páramo 1998; Papaderos & Östlin 2012) and SBS 0335-052W for which $12+\log(\text{O}/\text{H}) \approx 7.0-7.2$ (e.g., Izotov et al. 2009). Local metal-poor objects can be considered as template systems that help us to understand distant star-forming galaxies which cannot be studied to the same depth and angular resolution.

Wolf-Rayet (WR) signatures (most commonly a broad feature centered at $\sim 4680 \text{ \AA}$ or blue bump), indicating the pres-

* E-mail: kehrig@iaa.es

ence of WR stars (the last observable stage during the evolution of massive stars before the formation of neutron stars or black holes; e.g. Crowther 2007), have been found in the spectra of some HII galaxies (e.g., Kunth & Sargent 1981; Legrand et al. 1997; Guseva, Izotov, & Thuan 2000; Pérez-Montero et al. 2010). This is an important observational fact since single star, non-rotating stellar evolution models fail in reproducing the WR content in low metallicity environments (see Brinchmann, Kunth, & Durret 2008, and references therein). The investigation of the WR content in galaxies is crucial to test stellar evolutionary models, specially at low metallicities where more data are needed to constrain these models.

This work is part of our program to investigate HII galaxies with WR features using integral field spectroscopy (IFS; Kehrig et al. 2008; Pérez-Montero et al. 2011). IFS has many benefits in a study of this kind. Long-slit observations may fail in detecting WR features due to their faintness with respect to the stellar continuum emission and spatial distribution of WR stars across the galaxy. In particular in low metallicity objects, like HII galaxies, the dilution of WR features and the difficulty in spectroscopically identifying WR stars is even stronger owing to the steeper metallicity dependence of WR star winds which lowers the line luminosities of such stars (e.g., Crowther & Hadfield 2006). Kehrig et al. (2008) demonstrated for the first time the power of IFS in minimizing the WR bump dilution and finding WR stars in extragalactic systems where they were not detected before (see also Cairós et al. 2010; García-Benito et al. 2010).

This technique also lowers the difficulty when studying the spatial correlation between WR stars and properties of the surrounding interstellar medium (ISM; e.g., Legrand et al. 1997; de Mello et al. 1998). Massive stars play a key role in the evolution of the ISM. The mechanical energy injected by evolving stars through winds and supernova (SNe) explosions can reach values $\sim 10^{52}$ erg (e.g., Mollá, García-Vargas, & Bressan 2009). The spatial distribution of gas near the massive star clusters hosting WR stars may be affected by the disruption of the ISM, which also determines how newly synthesized metals are dispersed and mixed with the original gas from which the stars formed. Thus, a two-dimensional analysis of the ionized material in HII galaxies helps us to better understand the interplay between the massive stellar population and the ISM. For instance whether WR stars are a significant contributor to abundance fluctuations on timescales of $t \sim 10^7$ yr and to the formation of high-ionization lines (e.g. HeII λ 4686) are still unsolved issues (e.g., Roy & Kunth 1995; Kehrig et al. 2011; Shirazi & Brinchmann 2012) that can be probed more precisely when applying IFS to nearby galaxies like Mrk 178, as we will show in this manuscript. The investigation on formation and whereabouts of gamma-ray bursts and Type Ib/c supernova progenitors, believed to be WR stars in metal-poor galaxies, may also benefit from the study presented here (e.g., Woosley & Bloom 2006; Modjaz et al. 2008).

The presence of a broadened 4686 Å feature, attributable to WR stars, in the integrated spectrum of Mrk 178 had already been noticed by Gonzalez-Riestra, Rego, & Zamorano (1988). This system also appears in the WR galaxy catalogue by Schaerer, Contini, & Pindao (1999) and is contained in some studies of WR galaxies based on long-slit spectroscopy (e.g., Guseva, Izotov, & Thuan 2000; Buckalew, Kobulnicky, & Dufour 2005; Brinchmann, Kunth, & Durret 2008). In this work we present the first two-dimensional spectroscopic study of the close-by HII galaxy Mrk 178. At a distance of 3.9 Mpc (Karachentsev et al. 2003) and with a metallicity $\sim 1/10Z_{\odot}$, Mrk 178 is one of the most

Table 1. General Properties of Mrk 178

Parameter	Mrk 178 ^a
Other designation	UGC 06541
Morphological type ^b	ii,M dwarf
R.A. (J2000.0)	11h 33m 28.9s
DEC. (J2000.0)	+49d 14' 14"
redshift	0.0008
D ^c (Mpc)	3.9
Scale (pc//)	19
(B-R) ^d	0.89 ± 0.10
u^e (mag)	15.133 ± 0.040
g^e (mag)	14.228 ± 0.024
r^e (mag)	14.139 ± 0.023
i^e (mag)	14.131 ± 0.023
z^e (mag)	14.153 ± 0.021
A_V^f (mag)	0.049
R_{25}^g (arcmin)	0.62
$SFR(H\alpha)^h$ ($M_{\odot} \text{ yr}^{-1}$)	0.0085
Σ_{SFR}^i ($M_{\odot} \text{ yr}^{-1} \text{ Kpc}^{-2}$)	0.006

^a Mrk 178 belongs to the Markarian lists of galaxies with strong ultraviolet continuum (Markarian 1969); ^b From Gil de Paz et al. (2003); ^c Distance based on the tip of the Red Giant Branch distance from Karachentsev et al. (2003); ^d From Gil de Paz & Madore (2005); ^e SDSS photometry from Shirazi & Brinchmann (2012); ^f Galactic extinction from Schlegel et al. (1998); ^g The optical radius R_{25} ($= D_{25}/2$) in arcminutes, from the RC3 catalog (De Vaucouleurs et al. 1991); ^h The $H\alpha$ star formation rate from Lee et al. (2009); ⁱ Star formation rate per unit area [$= SFR/(\pi \times (R_{25})^2)$].

metal-poor nearby WR galaxies, which makes it an ideal object for our project.

We focus on investigating the spatial distribution of nebular physical-chemical properties (e.g. electron temperature, gaseous metal abundances) and excitation sources for the gas in Mrk 178, and how these are related with the WR content derived here. We discuss the significance of the observed spatial variations of electron temperatures and chemical abundances found here, and the origin of the nebular HeII λ 4686 emission. Additionally, Brinchmann, Kunth, & Durret (2008) found Mrk 178 to be an intriguing object and significant outlier among their sample of WR galaxies from the Sloan Digital Sky Survey (SDSS; York et al. 2000). Based on the SDSS spectrum of Mrk 178, the authors measured a remarkably high $L(\text{WR bump})/L(H\beta) \approx 0.05$. This corresponds to a $N(\text{WR})/N(\text{O}) \sim 0.5$ which is much higher than expected from any model at the low metallicity of Mrk 178. They suggested that this could be caused by the limited aperture size probed by the SDSS spectrum but were unable to test this possibility. In this work we test this hypothesis using our integral field unit (IFU) data. Table 1 compiles general properties of Mrk 178. In Fig. 1 we show a three-color broad band image from the SDSS of Mrk 178, and the HST/WFC3 image of Mrk 178 in the continuum filter F547M.

The paper is organized as follows. In Sect. 2, we report observations and data reduction. The WR content and nebular properties across the sampled regions of Mrk 178 are presented and discussed in Sect. 3. Finally, Sect. 4 summarizes the main conclusions derived from this work.

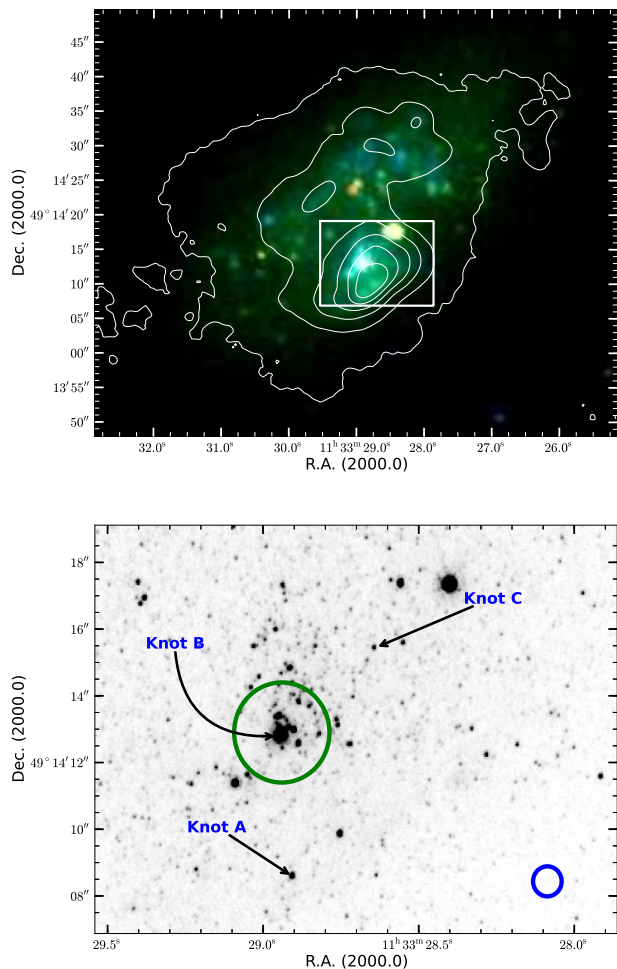


Figure 1. *Top:* Three-band (z,r,i) SDSS color-composite image of Mrk 178 overlaid with the observed field of view (FOV) of WHT/INTEGRAL ($\sim 16'' \times 12''$) represented by the white box. The $H\alpha$ contours from Gil de Paz, Madore, & Pevunova (2003) are also shown. *Bottom:* HST/WFC3 image of Mrk 178 in the continuum filter F547M, corresponding to WHT/INTEGRAL FOV. The big (green) circle represents the approximate location of the SDSS fiber on Mrk 178. The small (blue) circle illustrates an individual spaxel (spatial element on the IFU) from the INTEGRAL fiber system. The three WR knots defined in section 3 are also marked. North is up and east is to the left.

2 OBSERVATIONS AND DATA REDUCTION

2.1 Observations

IFS data of Mrk 178 were obtained with the INTEGRAL fiber system (Arribas et al. 1998) in combination with the WYFFOS spectrograph (Bingham et al. 1994) at the 4.2 m William Herschel Telescope (WHT), Roque de los Muchachos observatory. The data were taken with the 1024x1024 Tek6 CCD (Noise = 7 e; Gain = 2.1 e/ADU). The observations were performed on 2001 January 18 under photometric conditions and atmospheric extinction in r' of ~ 0.076 mag.

We used the R600B grating which covers from ~ 3710 to 6750 Å and provides a full width at half-maximum (FWHM) spectral resolution of ~ 6 Å and a linear dispersion ~ 3 Å/pixel. The data were taken with the standard bundle 2, for which the field-of-view (FOV) is formed by 189 fibers (each $\sim 0.9''$ in diameter) covering an area

of $16'' \times 12''$ (~ 300 pc \times 230 pc at the distance of 3.9 Mpc) on the sky (see Fig. 1). One pointing of Mrk 178, encompassing its major star forming region towards the south, was observed during 1.5 hours split into three exposures of 1800 seconds each. The science frames were taken at airmasses ≤ 1.1 in order to avoid strong effects due to differential atmospheric refraction.

Additionally, calibration images (exposures of arc lamps and of continuum lamps) were obtained. Observations of the spectrophotometric standard star Feige 34 were obtained during the observing night to flux calibrate the data.

2.2 Data Reduction

The first steps of the data reduction were done through the P3d tool which was developed to deal with integral-field spectroscopy data (Sandin et al. 2010). After subtracting the bias level, the expected locations of the spectra were traced on a continuum-lamp exposure. The spectra were wavelength calibrated using the exposures of CuAr+CuNe arc lamps obtained immediately after the science exposures. We checked the accuracy of the wavelength calibration by measuring the central wavelength of the $[O\text{I}]\lambda 5577$ Å sky line in all fibers and found a standard deviation of ± 0.20 Å.

Fibers have different transmissions that may depend on the wavelength. The continuum-lamp exposures were used to determine the differences in the fiber-to-fiber transmission and to obtain a normalized fiber-flat image, including the wavelength dependence. In order to homogenize the response of all the fibers, we divided our wavelength-calibrated science images by the normalized fiber-flat image.

In the next step, the three exposures taken for the same pointing were combined in order to remove cosmic rays, using the IMCOMBINE routine in IRAF¹. Flux calibration was performed using the IRAF tasks STANDARD, SENSFUNC and CALIBRATE. We co-added the spectra of the central fibers of the standard star exposure to create a 1D spectrum that was used to obtain the sensitivity function. This sensitivity function was applied to the combined Mrk 178 science frame.

3 RESULTS AND DISCUSSION

3.1 Number and location of WR stars

WR stars represent a late evolutionary phase of massive O stars whose initial mass (M_{ini}) on the main sequence was, at solar metallicity, $\gtrsim 25 M_{\odot}$. At lower metallicities, this M_{ini} limit increases (e.g. Crowther 2007). According to de Mello et al. (1998), the M_{ini} is $\gtrsim 90 M_{\odot}$ for $Z \sim 1/30 Z_{\odot}$, based on non-rotating models for single stars. Nevertheless, a significant number of WR stars detected in very metal-poor objects appears contrary to the expectations of such models (e.g. Izotov et al. 1997; Papaderos et al. 2006). Including rotation in the massive stellar evolution lowers the minimum mass required for a star to enter the WR phase, increasing their population in metal-poor environments (Meynet & Maeder 2005). WR stars are also extremely hot and luminous with temperatures that sometimes exceed 50,000 K and some with luminosities approaching $10^6 L_{\odot}$ (Crowther 2007). The

¹ IRAF is distributed by the National Optical Astronomical Observatories, which are operated by the Association of Universities for Research in Astronomy, Inc., under cooperative agreement with the National Science Foundation

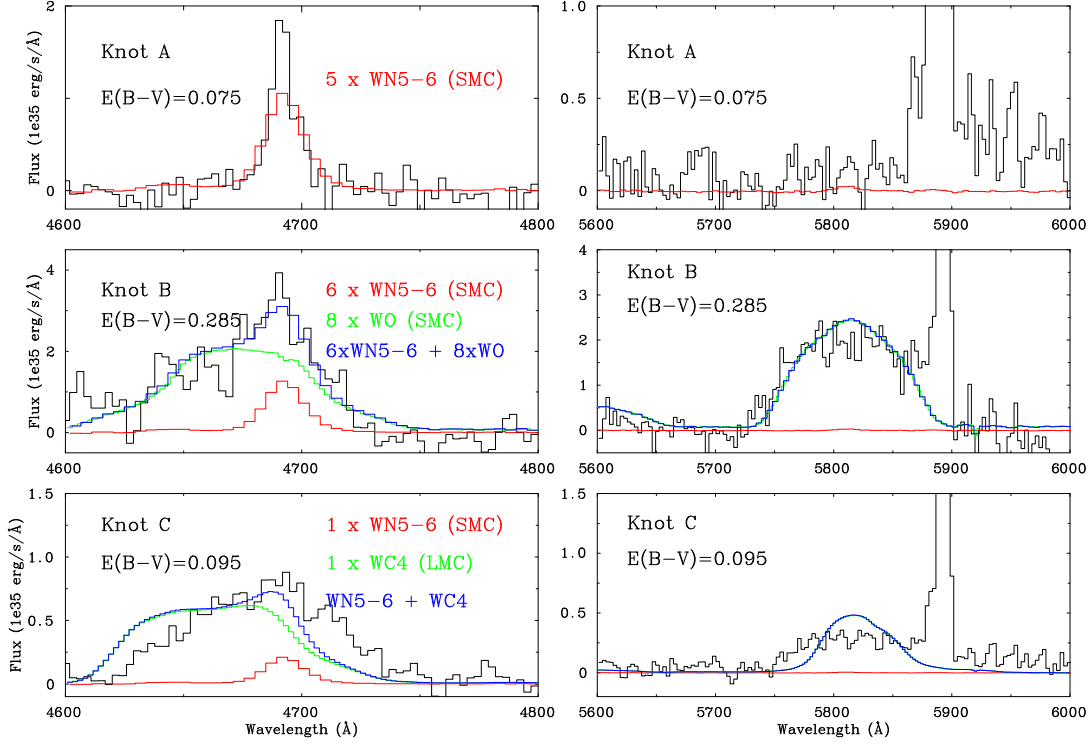


Figure 3. From top to bottom: dereddened spectra of knots A, B, and C (black lines), corrected for a distance of 3.9 Mpc. Generic blue and red WR features [WN templates (red lines); WC/WO templates (green lines); composite WN+WO/WC templates (blue lines)] are shown for comparison. Templates of SMC WR stars are used where possible (WN,WO). We adopt WC4 LMC template since no SMC counterparts are available. The spectra of the WR knots and WR star templates are continuum subtracted.

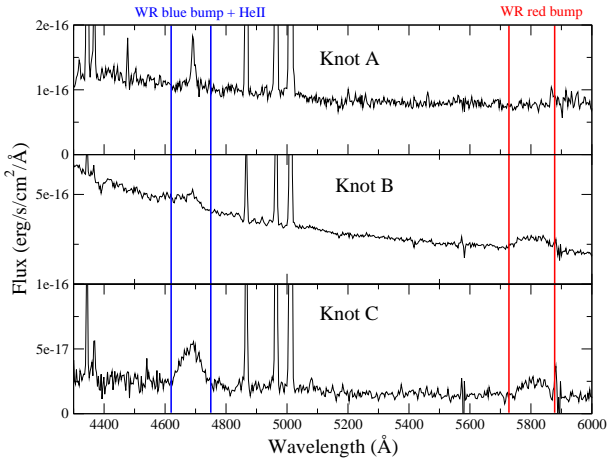


Figure 2. Portion ($\sim 4300 - 6000 \text{ \AA}$) of the integrated spectrum, in units of $\text{erg s}^{-1} \text{cm}^{-2} \text{\AA}^{-1}$, for the three knots in which the WR features are detected (see Figs. 5, 7 and 8). The spectral range for both blue and red WR bumps are marked.

spectra of WR stars show strong, broad emission lines formed in their fast, dense winds. Two main classes of WR stars are defined based on emission line ratios: nitrogen-type (WN) and carbon-type (WO and WC) stars (e.g., Smith, Shara, & Moffat 1996; Crowther, De Marco, & Barlow 1998). The so-called WN types are nitrogen-rich helium stars that show the results of the CNO hydrogen burning cycle (Smith 1973). Besides the classic He-burning WN stars, we also find in the literature examples of H-rich WR stars usually very luminous (WNh; Smith, Shara, & Moffat 1996;

Foellmi, Moffat, & Guerrero 2003; Schnurr et al. 2008) which are believed to be core-H burning (e.g. Crowther et al. 1995). Neither H nor N are detected in the spectra of carbon-type stars which show predominantly the products of the triple- α and other helium burning reactions (see Crowther 2007).

Integrated spectra of star-forming galaxies sometimes reveal WR spectral features, called WR bumps, which allow WR stars to be identified in both Local Group and more distant systems. Exhaustive searches for extragalactic WR stars have been the subject of several works (e.g., Buckalew, Kobulnicky, & Dufour 2005; Crowther et al. 2007; Neugent & Massey 2011). The blue and red WR bumps observed in galaxy spectra are centered at ~ 4680 and 5808 \AA , respectively. While WN stars are mainly responsible for the formation of the blue bump, the carbon-type WR stars contribute the most for the red bump emission.

WR features in the spectrum of Mrk 178 have been reported in previous work (Gonzalez-Riestra, Rego, & Zamorano 1988; Schaerer, Contini, & Pindao 1999; Guseva, Izotov, & Thuan 2000). From our IFU data we detect WR features in three different regions in the galaxy which we defined as WR knots (the location of the WR knots are marked on all maps of line intensity, line ratio and ISM properties; see Figs. 5, 7 and 8). Knots A and B are composed by three spaxels² while knot C is represented by a single spaxel. The detection of WR signatures at the locations of knots A and C is reported for the first time in this work. We created

² Individual elements of IFUs are often called 'spatial pixels' (commonly shortened to 'spaxel'); the term is used to differentiate between a spatial element on the IFU and a pixel on the detector.

one-dimensional spectra for knots A and B by adding the emission from the corresponding spaxels. Portions of the resulting spectra are shown in Fig. 2 from which we can see the WR signatures. The spectrum of knot A only displays the blue WR bump while we see both blue and red WR bumps in knots B and C. No WR features were detected in any parts other than Knots A, B and C across the sampled regions. We shall now discuss the WR content in Mrk 178 within the INTEGRAL FOV.

According to Starburst 99 synthesis evolutionary models (Leitherer et al. 1999) the expected number of WR stars for a star cluster at an age of ~ 4 Myr (the age at which models predict the WR content to be maximum), and with the $H\alpha$ luminosity ($\sim 10^{37}$ erg/s) and metallicity similar to those measured for the three WR knots in Mrk178 is $\lesssim 1$. State of the art models of stellar evolution that include the effects of rotation or binary evolution on the main sequence and beyond might be able to reproduce the observed WR features (e.g., Eldridge & Stanway 2009, and references therein). However, since full sets of tracks are not yet available and star forming regions do not fully sample the upper IMF, a more empirical approach has been taken. In this regard, we will use template fitting of individual WR stars to estimate the WR star content in this work. This methodology has been successfully applied in synthesizing the WR bumps in nearby spiral and irregular galaxies (e.g., Sidoli, Smith, & Crowther 2006; Hadfield & Crowther 2006; Moll et al. 2007) including one example for a metal-poor $[12+\log(\text{O}/\text{H}) \lesssim 8.0]$ HII galaxy (IZw18; Crowther & Hadfield 2006).

Here, to assess the number of WR stars in each knot, based upon currently available templates, we use SMC $[12+\log(\text{O}/\text{H}) \approx 8.0]$; Russell & Dopita (1990)] template WR stars [early-type WN (WN2-4), mid-type WN (WN5-6) from Crowther & Hadfield (2006); WO from Kingsburgh, Barlow, & Storey (1995)] because of the low metallicity of Mrk 178 $[12+\log(\text{O}/\text{H}) \approx 7.72]$; see section 3.2.3]. LMC templates are used solely when SMC templates are unavailable (e.g. WC subtypes). These template WR stars were adjusted for the redshift of Mrk 178 (250 km s^{-1}).

Figure 3 shows the comparison between the observed WR bumps for our 3 knots and the WR template spectra [predictions for WN stars (red), WC/WO stars (green) and composite WN+WC/WO stars (blue)]. In view of the limited templates available and variations in line strength and line width for individual WR stars we wish to emphasise that the results presented here are not unique, but that we attempt to match the morphology (line strength and width) using the fewest number of subtypes.

In Knot A, a broad blue ($\lambda_c \sim 4686$; FWHM $\sim 15 \text{ \AA}$) emission feature is observed, together with possible nebular $\text{HeII}\lambda 4686$ component. The FWHM ($\sim 5 \text{ \AA}$) of this narrow HeII component, comparable to that of the other nebular emission lines (e.g., $[\text{O III}]\lambda 5007$), and its spatial extent are evidence of its nebular nature. Applying the SMC WN calibration from Crowther & Hadfield (2006) to the blue bump would require \sim five equivalent WN5-6 stars.

For knot B, we estimate that six WN5-6 and eight WO stars [$\text{CIV}\lambda 5808$ is very broad (FWHM $\sim 100 \text{ \AA}$) requiring a WO instead of WC template] are needed to reproduce the WR features. The blue WR spectral feature in knot C is fairly well reproduced by a population of 1 SMC-like WN5-6 star and 1 LMC-like WC4 star (LMC template WC4 stars were used since no WC4 have been observed in the SMC). However the broad red feature requires a WO star to match the observed morphology, while the blue comparison

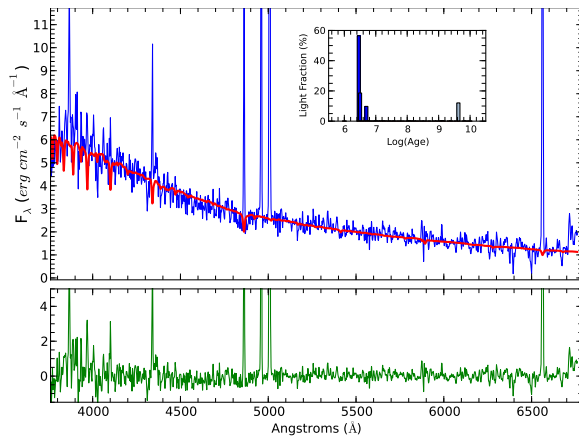


Figure 4. This figure illustrates the main output from spectral synthesis for a single spaxel ($\sim 1''$ from Knot B) in the region of Mrk 178 sampled in this work. The blue and red lines (top panel) correspond to the observed spectrum and the best-fitting synthetic SED for the stellar continuum, calculated with the population synthesis code STARLIGHT, respectively. By subtracting the latter from the former we obtain the pure nebular emission line spectrum (green in the bottom panel). The y-axis is in $10^{-17} \text{ erg s}^{-1} \text{ cm}^{-2} \text{ \AA}^{-1}$. The smaller panel shows the age distribution of the stellar populations in the best-fitting synthetic SED as a function of their luminosity (at 4200 \AA) in percent.

is much worse. Alternatively, we checked whether a WN/C star³ might enable a match to both blue and red features simultaneously, but a satisfactory solution could not be achieved since both features are much too broad with respect to a WN/C star. While the small number of appropriate templates from the SMC means that we cannot achieve a perfect fit for knot C, we find that a population of $\sim 1-2$ WR stars is likely.

Of course, one needs to bear in mind that the numbers of WR stars implied from these comparisons are only as good as the templates used. For instance, there are only two carbon sequence WR stars at metallicities below the LMC in the Local Group: the WO stars DR1 in IC 1613 (Kingsburgh & Barlow 1995) and Sand 1 in the SMC (Kingsburgh, Barlow, & Storey 1995). In view of this, we have also examined the DR1 template, but the width of the red bumps observed in knots B and C is in much better agreement with the SMC template. In addition, the use of LMC templates for WC stars (in the absence of SMC counterparts) is clearly not ideal. Still, the morphology of WC stars in the metal-poor dwarf IC 10 is reminiscent of the LMC. Indeed, the average $\text{C IV } \lambda 5801-12$ line luminosity of IC 10 WC stars is consistent with that of the LMC WC population, in spite of large uncertainties due to high foreground interstellar extinction (Crowther et al. 2003).

Early-type WN templates would indicate a larger WR population (factor of ~ 10 times higher than for mid-type WN stars), although we prefer mid-type WN stars throughout to early-WN stars because they provide a better match to the $\text{HeII}\lambda 4686$ line width. Of course, individual WN stars at a given subtype span a range of line widths, but the range is modest for mid- and late-type stars (see Fig.2 from Crowther & Hadfield 2006).

In addition to the observed line width constraint, mid-WN stars tend to be especially common in giant HII regions across a range of metallicities, including our Milky Way (e.g.,

³ Our template, Brey 29 (BAT99-36), is the LMC composite WN4b/WCE (Foellmi, Moffat, & Guerrero 2003)

NGC 3603; Drissen et al. 1995), the LMC⁴(e.g. 30 Doradus; Moffat, Seggewiss & Shara 1985); and the SMC (e.g. NGC 346; Conti, Garmany, & Massey 1989). Therefore, we might expect these to dominate over early WN stars in knots A and B for which the spatial extent is ~ 4 arcsec (~ 80 pc at a distance of ~ 4 Mpc), the size of typical HII regions. The size of Knot C (radius ~ 8 pc) is of the order of some ejecta nebulae around isolated/binary WR stars (e.g., Esteban & Vilchez 1992; Stock & Barlow 2010; Fernández-Martín et al. 2012) which supports our estimation of very few WR stars (~ 1 -2) there. It is likely that the number of WR stars estimated here represents a lower limit owing to the use of SMC templates and reduced line luminosities at lower metallicities (Crowther & Hadfield 2006). Unfortunately, a more quantitative assessment would require more individual metal-poor WR stars to be included in low metallicity templates (IC10 is the only suitable candidate at the present time).

3.2 A 2D view of the warm ISM

3.2.1 Line fitting and map creation

To derive line ratios properly, we first subtracted from the observed spectra the spectral energy distribution (SED) of the underlying stellar population found by the spectral synthesis code STARLIGHT⁵ (Cid Fernandes et al. 2004, 2005; Mateus et al. 2006). STARLIGHT fits an observed continuum SED using a combination of the synthesis spectra of different single stellar populations (SSPs) using a χ^2 minimization procedure. We chose for our analysis the SSP spectra from Bruzual & Charlot (2003), based on the STELIB library of Le Borgne et al. (2003), Padova 1994 evolutionary tracks and a Chabrier (2003) initial mass function between 0.1 and 100 M_{\odot} . We used the library metallicities ($Z=0.001, 0.004, 0.008$) closest to the average oxygen abundance measured in the gas [$12+\log(O/H) \approx 7.72$; see Section 3.2.3] and a set of 38 ages from 1 Myr up to 10 Gyr. The reddening law from Cardelli et al. (1989) with $R_V = 3.1$ was applied. Bad pixels and emission lines were excluded from the final fits. According to the model SSPs, the correction factor for stellar absorption in the EW(H β) is $\sim 10\%$ on average. Our nebular lines have EW(H β) > 10 Å so the effect of the underlying stellar population in Balmer lines involved in the reddening derivation is negligible. The best spectral synthesis fits also show that young stellar populations (age $< 10^7$ yrs) dominate the light fraction in most spaxels. An illustrative example of the observed, modeled, and emission-line spectrum for a single spaxel in the FOV of Mrk 178 is displayed in Fig. 4.

After subtracting the underlying stellar population for each spaxel spectrum, the emission-line fluxes are measured using the IRAF task `splot`. The intensity of each emission line was derived by integrating between two points given by the position of a local continuum placed by eye. The line-flux errors were calculated using the following expression:

$$\sigma_{line} = \sigma_{cont} N^{1/2} \left(1 + \frac{EW}{N\Delta\lambda} \right)^{1/2} \quad (1)$$

where σ_{cont} is the standard deviation of the continuum near the emission line, N is the width of the region used to measure the

line in pixels, $\Delta\lambda$ is the spectral dispersion in Å/pixel, and EW represents the equivalent width of the line (Gonzalez-Delgado et al. 1994). This expression takes into account the error in the continuum and the photon count statistics of the emission line⁶. The relative errors in the line intensities are ~ 5 -8% for the bright lines (e.g. [OII] $\lambda 3727$; [OIII] $\lambda 5007$; H α). Typical uncertainties for the weakest lines ([OII] $\lambda 4363$; HeII $\lambda 4686$; [NII] $\lambda 6584$) are about $\sim 15\%$ and may reach up to ~ 20 -30% in some fibers. The final errors do not account for flat-field and instrumental response uncertainties which are not significant ($< 5\%$).

Using our own IDL scripts we combine the flux intensities with the sky position of the fibers to create the maps of emission lines and line-ratios presented in this paper. Figure 5 displays flux maps of some of the relevant emission lines and line ratios. As a guide to the reader, the spaxels where we detect WR signatures are indicated in all maps. The H α and [OII] $\lambda 3727$ maps show a larger area than the HeII $\lambda 4686$ map because those lines are among the brightest optical emission lines in our data sets. The maps of [OII] $\lambda 3727$ /H β and [OIII] $\lambda 5007$ /H β present opposite trends; [OII] $\lambda 3727$ /H β peaks in the outer zones of the FOV while the highest values of [OIII] $\lambda 5007$ /H β are observed close to the WR knot thereabouts where the ionizing flux should be harder (see section 3.2.4 for discussion on excitation sources). The map of the [OII] $\lambda 3727$ /[OIII] $\lambda 5007$ ratio which is an indicator of the ionization parameter, is also shown. In addition, Fig.6 displays the H α map along with representative emission-line spectra from spaxels in different positions across our FOV.

3.2.2 Physical conditions and chemical abundances in the ISM

The reddening coefficient corresponding to each fiber spectrum, $c(H\beta)$, was computed from the ratio of the measured-to-theoretical H α /H β assuming the reddening law of Cardelli et al. (1989), and standard HII region characteristics ($T_e = 10^4$ K; $n_e = 100$ cm³) which give an intrinsic value of H α /H β = 2.86 (Storey & Hummer 1995).

Using the de-reddened line-ratios, we derived the physical properties and ionic abundances of the ionized gas for Mrk 178 following the 5-level atom FIVEL program (Shaw & Dufour 1994) available in the tasks TEMDEN and IONIC of the STSDAS package. We calculated the final errors in the derived quantities by error propagation and taking into account errors in flux measurements. Systematic errors are not included.

We obtained the electron densities, n_e , from the [SII] $\lambda 6717$ /[SII] $\lambda 6731$ line ratio. The derived estimates and upper limits for n_e place all of spaxel spectra in the low-density regime ($n_e \lesssim 300$ cm³).

We derived the T_e values of [OII] using the [OII] $\lambda 4363$ /[OII] $\lambda 4959, 5007$ line ratio. T_e [OII] was calculated from the relation between [OII] and [OIII] electron temperatures given by Pérez-Montero & Díaz (2003) assuming an electron density of 100 cm⁻³. We measured the faint auroral line [OII] $\lambda 4363$ for 60 spaxels with S/N > 3 . These spaxels cover a projected area of nearly 42 arcsec² equivalent to ~ 0.02 kpc², including the central starburst region.

The oxygen ionic abundance ratios, O⁺/H⁺ and O²⁺/H⁺, were derived from the [OII] $\lambda 3727$ and [OIII] $\lambda 4959, 5007$ lines, respectively using the corresponding electron temperatures. The total

⁴ Crowther & Hadfield (2006) included 15 LMC WN5-6 stars in their mid-WN template, of which 7 lie within 30 Doradus (R144-147, R136a1, a2, a3).

⁵ The STARLIGHT project is supported by the Brazilian agencies CNPq, CAPES and FAPESP and by the FranceBrazil CAPES/COFECUB programme.

⁶ We caution that for faint stars near the detection limit CCD readout noise can also be important.

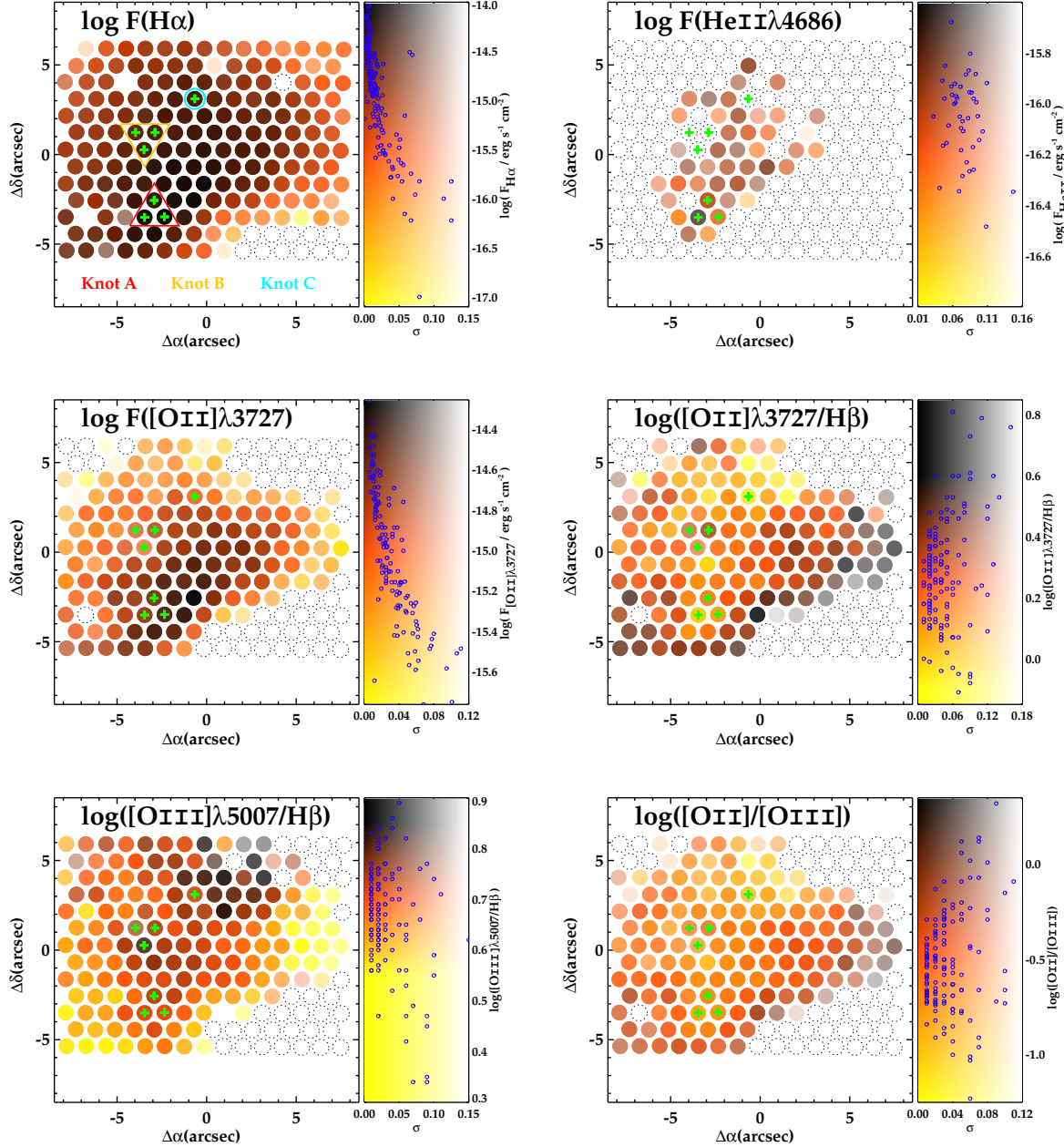


Figure 5. Intensity and line ratio maps of Mrk 178: $H\alpha$, narrow $\text{HeII}\lambda 4686$, $[\text{OII}]\lambda 3727$, $[\text{OII}]\lambda 3727/H\beta$, $[\text{OIII}]\lambda 5007/H\beta$ and $[\text{OII}]\lambda 3727/[\text{OIII}]\lambda 5007$. Dotted circles show the spaxels where no measurement is available. All maps are presented in logarithmic scale. The three WR knots (A, B and C) are labeled on the $H\alpha$ flux map, and the spaxels where we detect WR features are marked with green crosses on all maps. For each map the vertical axis of the right-hand side color bars represents the values of the corresponding line (-ratio) while the horizontal axis (σ) displays the uncertainties associated with each quantity, which are coded using an α -channel (transparency of the spaxel color). According to the α -channel coding, the more intense the color the lower the uncertainty. North is up and east to the left.

oxygen abundance is assumed to be: $\text{O}/\text{H} = \text{O}^+/\text{H}^+ + \text{O}^{2+}/\text{H}^+$. With regards to the oxygen ionization correction factor (ICF), a small fraction of O/H is expected to be in the form of the O^{3+} ion in high excitation HII regions when $\text{HeII}\lambda 4686$ emission line is detected. In our case, we find the correction for the unseen higher ionization stages of oxygen to be negligible; in the spaxels where we measure $\text{HeII}\lambda 4686$, the $\text{ICF}(\text{O})$ correction would increase the total O/H by less than ~ 0.02 dex, which is considerably lower than the typical error associated with our O/H measurements (see top-left panel of

Fig. 7). N^+ abundances were derived using the $[\text{NII}]$ emission line at 6584 \AA and assuming $T_e[\text{NII}] \sim T_e[\text{OII}]$; the N/O abundance ratio was derived under the assumption that $\text{N}/\text{O} = \text{N}^+/\text{O}^+$. Finally, based on the $\text{HeII}\lambda 6678$ and equations from Olive & Skillman (2004), we calculate He^+/H^+ . These equations were used for the appropriate values of n_e , temperature, and account for collisional deexcitation. We ignore $\text{HeII}\lambda 5876$ since it is affected by Galactic NaI absorption and $\text{HeII}\lambda 4471$ due to too low S/N.

We also derived O/H values based on the N2 param-

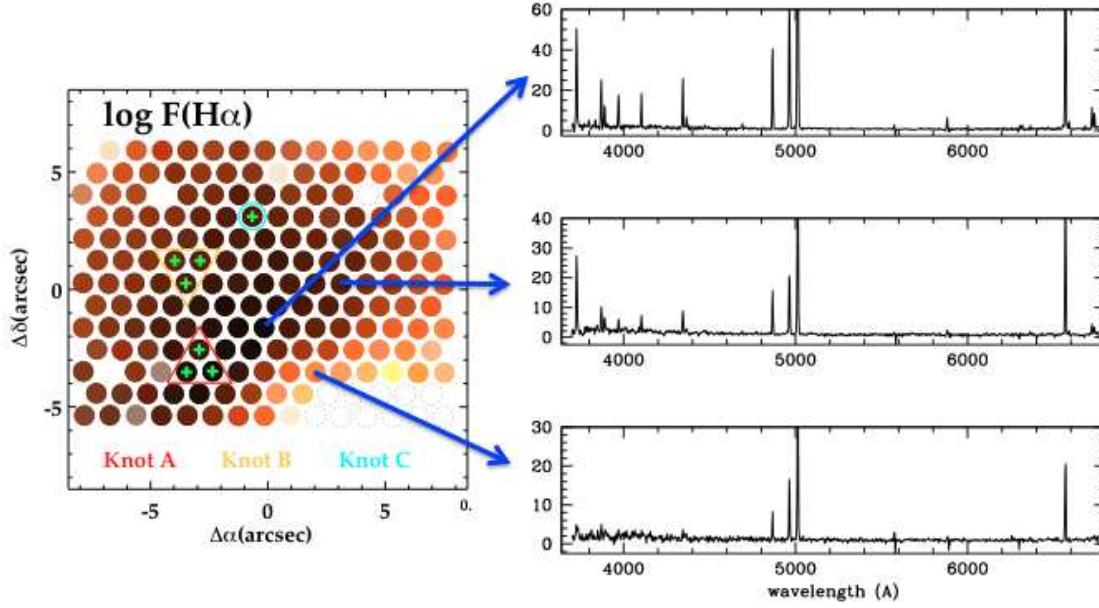


Figure 6. Representative spectra in units of $10^{-17} \text{ erg s}^{-1} \text{ cm}^{-2} \text{ Å}^{-1}$, corresponding to the nebular emission of three single spaxels across the FOV.

ter $[=\log([\text{NII}]\lambda 6584/\text{H}\alpha)]$ by Pérez-Montero & Contini (2009) to have an estimation of the metallicity over a larger number of spaxels. The N2 parameter is almost independent of reddening effects, and the relationship between N2 and O/H is single-valued. Moreover, to derive N/O in a larger spatial extent, we made use of the N2O2 parameter $[=\log([\text{NII}]\lambda 6584/[\text{OII}]\lambda 3727)]$ which has a linear relation with N/O at all ranges of metallicity (Pérez-Montero & Contini 2009).

Maps and histograms of the derived O/H and N/O are displayed in Figs. 7 and 8, respectively.

For the three WR knots A, B and C, the physical-chemical properties are derived following the methodology described above and are presented in Table 2.

3.2.3 Spatial variations of the ISM properties

Here, we refine the method described in Pérez-Montero et al. (2011) to study spatial variations of ISM properties based on statistical criteria. We assume that a certain physical-chemical property is homogeneous across our INTEGRAL FOV if two conditions are satisfied: for the corresponding dataset (i) the null hypothesis (i.e. the data come from a normally distributed population) of the Lilliefors test (Lilliefors 1967) cannot be rejected at the 10% significance level, and (ii) the observed variations of the data distribution around the single mean value can be explained by random errors; i.e. the corresponding Gaussian sigma (σ_{Gaussian}) should be of the order of the typical uncertainty of the considered property; we take as typical uncertainty the square root of the weighted sample variance (σ_{weighted}). In Table 3 we show the results from our statistical analysis for relevant ISM properties.

For the electron temperature, despite the fact that the distribution of its measured values can be represented by a Gaussian fit (based on the Lilliefors test), we find that $\sigma_{\text{Gaussian}} > \sigma_{\text{weighted}}$ (see Table 3). This suggests that as a first approximation random variables alone should not explain the T_e distribution. The

source of these variations is hard to assess. A possible explanation could be some error source that we do not take into account (e.g. variable seeing). However if this was the explanation, this source of error should affect all emission lines which does not seem to be the case. Our statistical study indicates that the scatter in T_e can be larger than the scatter in O/H within Mrk 178. Vílchez & Iglesias-Páramo (1998) find similar results for IZw18. The opposite is also found in the literature; i.e. chemically homogeneous gas is found in star-forming regions with no apparent T_e variation (e.g., Gonzalez-Delgado et al. 1996).

From Table 3 we find that the measured values of O/H, both from direct-method and N2 calibrator, are fitted by a normal distribution according to the Lilliefors test; additionally $\sigma_{\text{Gaussian}} \sim \sigma_{\text{weighted}}$ in both methods. We find the same results when considering only the O/H values from the spaxels where we measure the nebular $\text{HeII}\lambda 4686$ (gray bars in the histograms of Fig. 7). Thus, according to our statistical analysis, the oxygen abundance in the ISM of Mrk 178 is homogeneous over spatial scales of hundreds of parsecs. However, we must bear in mind that this statistical methodology ignores any spatial information and cannot be used to discard the presence of small-scale localized (~ 20 pc, our resolution element size) chemical variations, as we will discuss further in this section.

Close inspection of the two histograms in Fig. 7 indicates that the Gaussian fit for the distribution of $\text{O}/\text{H}_{\text{N2}}$ is slightly broader than that for the O/H_{T_e} histogram ($\sigma_{\text{Gaussian}, \text{N2}}=0.16$; $\sigma_{\text{Gaussian}, T_e}=0.12$), and the Gaussian peak is somewhat shifted towards higher values. This probably reflects the dependence of N2 on the ionization parameter. Still, the mean values of the corresponding $\text{O}/\text{H}_{\text{N2}}$ and O/H_{T_e} distributions are consistent within the errors (see Table 3).

In the case of the N/O ratio, the width and peak of the histograms for both $(\text{N}/\text{O})_{T_e}$ and $(\text{N}/\text{O})_{\text{N2O2}}$ values are similar (see Table 3 and Fig. 8). The distribution of N/O values can be represented by a Gaussian fit in agreement with the Lilliefors test, independently of the method used to estimate the N/O ratio. Also, σ_{Gaussian}

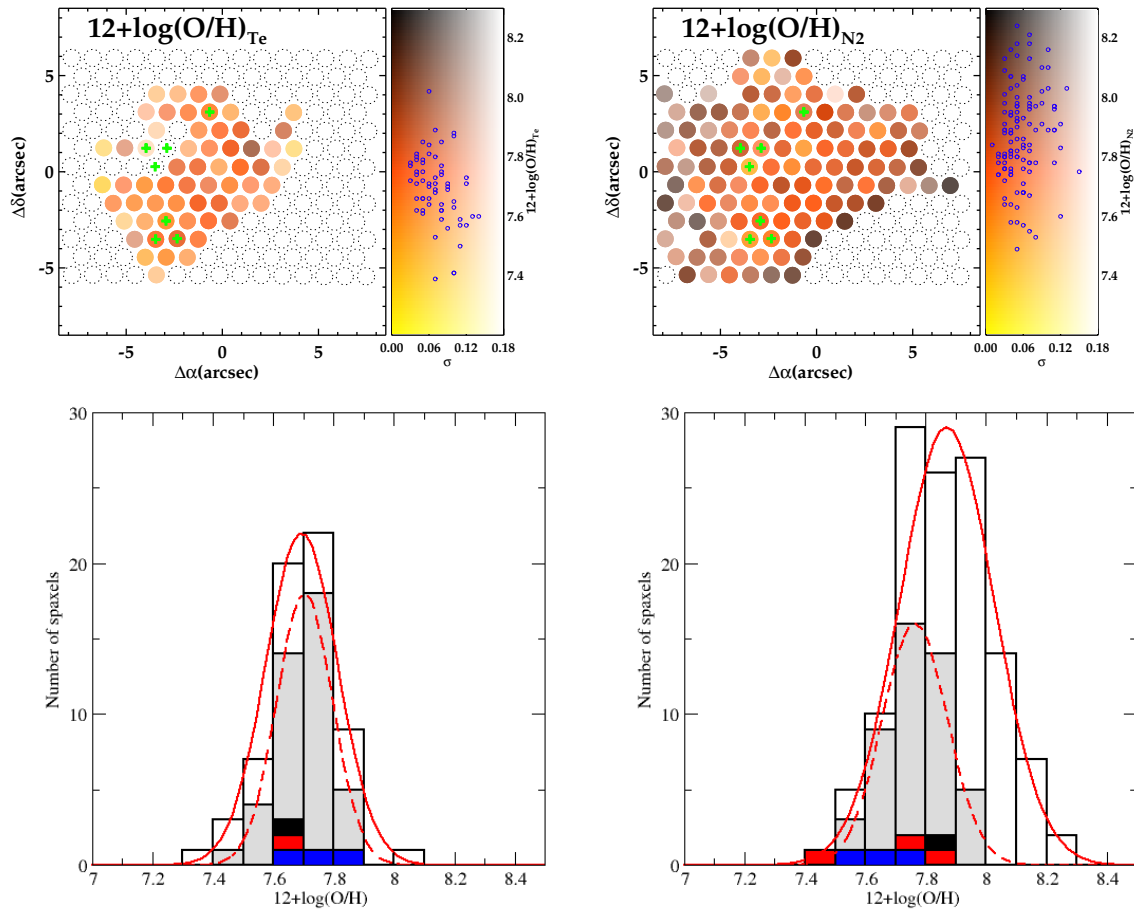


Figure 7. *Top panels:* maps of oxygen abundance ($12+\log \text{O}/\text{H}$) derived from $T_e[\text{OIII}]$ (left) and the N2 parameter (right); right-side color bars and green crosses are as indicated in Fig. 5. The corresponding histograms are in the *bottom row*. The gray bars indicate the spaxels where we measure the nebular $\text{HeII}\lambda 4686$, blue bars represent the spaxels showing only the blue WR bump (i.e. the spaxels within knot A; see Figs. 2 and 5), red bars indicate the spaxels within Knot B (see Figs. 2 and 5), all showing both the blue and red WR bumps, and the black bar represents the individual spaxel in the NW with both the blue and red WR bump detection (i.e. Knot C in Figs. 2 and 5). The solid and dashed curves are the Gaussian fits to all spaxels and only the spaxels where we detect nebular $\text{HeII}\lambda 4686$ line, respectively. The uncertainties of $(\text{O}/\text{H})_{\text{N2}}$ are obtained by propagating the errors of $[\text{NII}]$ and $\text{H}\alpha$ lines (involved in the N2 parameter) in the derivation of O/H , and do not consider the typical uncertainty associated with the N2 parameter (~ 0.3 dex).

is of the order of σ_{weighted} as is the case with O/H . Taking into account only the spaxels with nebular $\text{HeII}\lambda 4686$ detection (gray bars in the histograms of Fig. 8) yields the same results. So, overall, across the whole FOV (~ 300 pc \times 230 pc) of Mrk 178 we find no statistically significant variations in N/O .

Since our statistical analysis does not consider any particular spatial information, as mentioned above, to probe the existence of small-scale (~ 20 pc) localized chemical pollution, we have inspected the chemical abundances for the WR knots as derived in section 3.2.2 (see Table 2). From Table 2 and the N/O distributions in Fig. 8, we note that WR knot C appears to present a higher N/O . Since N enrichment from WR star winds is expected to come with He enhancement (e.g., Pagel, Terlevich, & Melnick 1986; Esteban & Vilchez 1992; Kobulnicky & Skillman 1996), we analyse the He^+/H^+ as well. From Fig. 9, the histogram of He^+/H^+ , and Table 2 one sees that WR knot C presents a considerably high He^+/H^+ (~ 0.18) in comparison to the rest of the spaxels. Thus, the existence of a localized N and He^7 pollution by WR stars

in knot C cannot be ruled out. Since Maeder (1992), it is well known that WR stars are significant contributors of He, N and C. At these small-scales, chemical enrichment has been previously reported for Galactic WR nebulae (e.g., Esteban & Vilchez 1992; Fernández-Martín et al. 2012) and for irregular dwarf galaxies, for instance IC 10 (López-Sánchez et al. 2011) and NGC 5253 (e.g., Kobulnicky et al. 1997; Monreal-Ibero, Walsh, & Vilchez 2012). A statistical detection of N enhancement in galaxies showing WR features has been reported by Brinchmann, Kunth, & Durret (2008). No evidence of chemical enrichment in the gas associated with the WR knots A and B is found. Nevertheless, one should bear in mind the detection of any chemical pollution on scales of \sim few parsecs will escape this work because of our resolution element size (~ 20 pc at the distance of Mrk 178).

Summarizing, chemically homogeneous ionized gas on spatial scales of $\gtrsim 100$ pc appears to be a rule in HII galaxies (e.g., Lee & Skillman 2004; Kehrig et al. 2008; Pérez-Montero et al.

⁷ Considering the high ionization degree of the WR knots (O^{++}/O is > 0.70

for the three WR knots), their corresponding $\text{ICF}(\text{He})$ is expected to be ~ 1 (Izotov, Thuan, & Stasińska 2007)

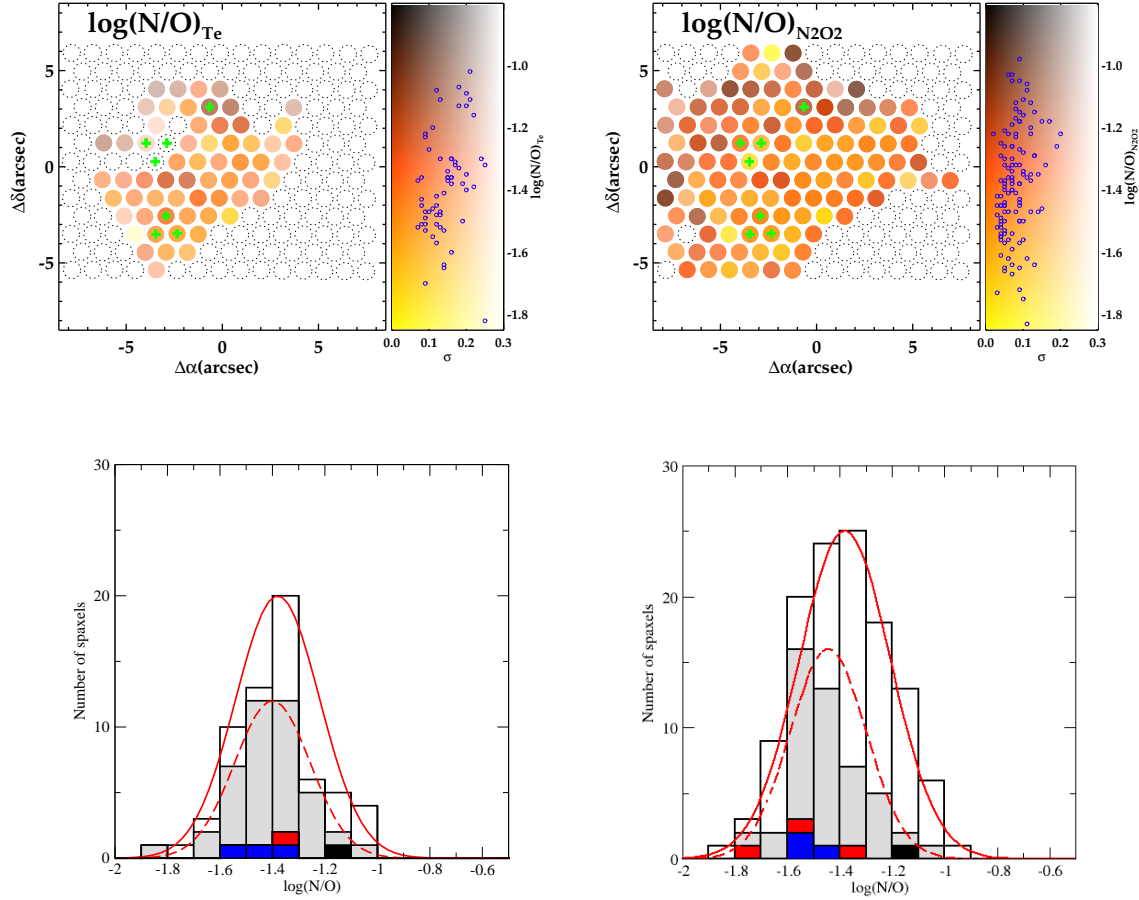


Figure 8. *Top panels:* maps of $\log(\text{N/O})$ derived from $T_e[\text{OIII}]$ (left) and the N2O2 parameter (right); right-side color bars and green crosses are as indicated in Fig. 5. The corresponding histograms are in the *bottom row*; the colouring of the bars and curves are the same as in Figure 7. The uncertainties of $(\text{N/O})_{\text{N2O2}}$ are obtained by propagating the errors of $[\text{NII}]$ and $[\text{OII}]$ lines (involved in the N2O2 parameter) in the derivation of N/O , and do not consider the typical uncertainty associated with the N2O2 parameter (~ 0.25 dex).

2009; Cairós et al. 2009a,b; Pérez-Montero et al. 2011; García-Benito & Pérez-Montero 2012). One may speculate that the ionized ISM in Mrk 178 and other HII galaxies appears presently well homogenized because the freshly synthesized elements were rapidly dispersed, on timescales $< 10^7$ yr, and mixed very quickly in the ISM. This hypothesis requires that ejected metals are both homogeneously dispersed and mixed with the ambient ISM on time scales comparable to that of the HII regions which seems to be unlikely based on hydrodynamical and physical processes in the gas (see Roy & Kunth 1995; Tenorio-Tagle 1996; Kobulnicky & Skillman 1997). Alternatively, the scenario proposed by Tenorio-Tagle (1996), in which the ejecta from stellar winds and supernovae could undergo a long (~ 100 Myr) cycle in a hot phase ($\sim 10^6$ K) before mixing with the surrounding ISM, has been discussed in the literature (e.g. Kobulnicky & Skillman 1997; van Zee & Haynes 2006) as a possible explanation for the homogeneous chemical appearance of HII galaxies on spatial scales of $\gtrsim 100$ pc. However the fate of the metals released by massive stars in HII regions is still an open question, and the processes of metal dispersal and mixing are very difficult to model (see Recchi et al. 2003; Recchi & Hensler 2013). Thus, to better understand how the ejected metals cool and mix with the ISM, further investigation

on the metal content of the different ISM phases is needed but is beyond the scope of this work (e.g. Leboutteiller et al. 2009).

In this work we find that the representative metallicity of Mrk 178 is $12 + \log(\text{O/H}) = 7.72 \pm 0.01$ ($\sim 1/10$ of the solar metallicity) which represents the derived error-weighted mean value of O/H and its corresponding statistical error from all the individual spaxel measurements obtained from the direct-method (for this O/H distribution, the square root of the weighted sample variance associated is 0.13 dex; see Table 3).

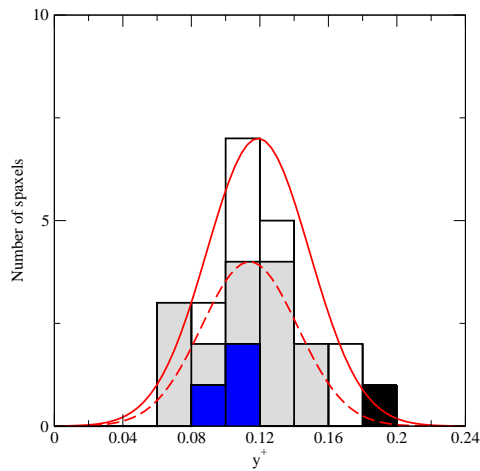
3.2.4 Excitation sources and nebular $\text{HeII}\lambda 4686$ emission

Although photoionization by massive stars is the most likely main excitation source in HII regions, some questions still remain regarding the origin of high-ionization nebular lines as for instance $\text{HeII}\lambda 4686$. This line has been observed in several WR galaxies, especially in the low-metallicity ones, like Mrk 178 (e.g., Schaerer, Contini, & Pindao 1999). A possible explanation for this is that in such metal-poor environments, WR stars possess sufficiently weak winds that are optically thin in the He^+ continuum (e.g., Schmutz, Leitherer, & Gruenwald 1992;

Table 2. De-reddened emission line-fluxes relative to 1000-I(H β) and physical properties for the WR knots. The properties of the WR bumps are quoted.

Wavelength	Knot A	Knot B	Knot C
3727 [O II]	1320 \pm 60	1670 \pm 110	955 \pm 60
4363 [O III]	135 \pm 14	112 \pm 17	147 \pm 12
4686 He II	40 \pm 4	—	—
4861 H β	1000 \pm 20	1000 \pm 90	1000 \pm 50
5007 [O III]	5290 \pm 160	5213 \pm 360	5330 \pm 180
6563 H α	2810 \pm 60	2810 \pm 240	2770 \pm 110
6584 [N II]	51 \pm 14	93 \pm 30	77 \pm 16
6678 HeI	37 \pm 6	—	63 \pm 16
6717 [S II]	112 \pm 5	132 \pm 11	129 \pm 15
6731 [S II]	68 \pm 5	89 \pm 9	102 \pm 16
c(H β)	0.16 \pm 0.03	0.26 \pm 0.10	0.14 \pm 0.05
-EW(H β) (Å)	80 \pm 2	9 \pm 1	33 \pm 5
log F(H β) (erg/s)	-14.00	-14.25	-14.75
n_e ([S II])(cm $^{-3}$)	<10	<10	210
T_e ([O III])	16186 \pm 675	14600 \pm 750	17079 \pm 530
12+log (O^+/H^+)	7.10 \pm 0.08	7.29 \pm 0.12	6.93 \pm 0.08
12+log (O^{++}/H^+)	7.65 \pm 0.05	7.76 \pm 0.07	7.60 \pm 0.03
12+log (N^+/H^+)	5.65 \pm 0.14	5.97 \pm 0.17	5.81 \pm 0.10
12+log (O/H) $_{T_e}$	7.76 \pm 0.06	7.89 \pm 0.08	7.69 \pm 0.09
log (N/O) $_{T_e}$	-1.45 \pm 0.16	-1.32 \pm 0.20	-1.12 \pm 0.13
He $^+$ /H $^+$ (λ 6678)	0.11 \pm 0.02	—	0.18 \pm 0.05
He $^{2+}$ /H $^+$ (λ 4686) a	0.004 \pm 0.001	—	—
log L(WR blue bump) b (erg/s)	36.60 \pm 0.07	37.52 \pm 0.06	37.22 \pm 0.07
-EW (WR blue bump) (Å)	7 \pm 2	8 \pm 2	50 \pm 12
log L(WR red bump) b (erg/s)	—	37.88 \pm 0.05	36.87 \pm 0.06
-EW (WR red bump) (Å)	—	20 \pm 6	55 \pm 15

(a) estimated from HeII λ 4686 and T_e ([OIII]) (Izotov, Thuan, & Lipovetsky 1994). (b) extinction-corrected luminosity of the WR bumps derived at our assumed distance of 3.9 Mpc; to measure the WR features we fitted the stellar continuum using a polynomial function and we subtracted it from the WR emission. Nebular HeII λ 4686 line was removed before deriving the luminosity and EW of WR blue bump for knot A.


Figure 9. Histogram of the He $^+$ /H $^+$ ionic abundance ratio; the colouring of the bars and curves are the same as in Figure 7.

Crowther & Hadfield 2006), therefore allowing the He $^+$ -ionizing photons to escape from the stellar atmospheres.

However, WR features are not always seen when nebular HeII is observed. The nebular emission of HeII λ 4686 detected in this work is shown to be spatially extended, and some HeII-emitting

regions are not coincident with the location of the WR bumps by tens of parsecs (see the map of HeII λ 4686 in Fig. 5). Similar results have been found in previous work. In Kehrig et al. (2008) a spatial separation between the WR star thereabouts and the HeII emission is found to be ~ 80 pc in the HII galaxy IIZw70. More recently, Shirazi & Brinchmann (2012) studying a sample of star-forming galaxies with nebular HeII emission from SDSS DR7 find that a large fraction of the objects at low metallicities do not show WR signatures. Kehrig et al. (2011) also identify two HeII nebulae in M33 which do not appear to be associated with any WR star.

Different ionizing mechanisms other than WR stars (e.g. shocks; X-ray binaries) for the formation of the HeII line have been discussed in the literature (e.g., Garnett et al. 1991; Shirazi & Brinchmann 2012). Shocks do not seem to be an important excitation source in Mrk 178 at large since this galaxy is not detected in X-rays (Stevens & Strickland 1998), indicating that shock-ionization should not be responsible for the HeII emission. Our measured values of [SII] $\lambda\lambda$ 6717,6731/H α ratio ($\lesssim 0.20$) are lower than the ones observed in SNRs ([SII] $\lambda\lambda$ 6717,6731/H α $\sim 0.5 - 1.0$; Smith et al. 1993] which points against shock ionization as well. The lack of X-ray detection also leads us to consider X-ray binaries not to be the main source of He $^+$ ionization.

Can we still associate the nebular HeII in Mrk 178 with its WR stars despite the spatial offset between the location of the WR stars and the HeII-emitting zones? To answer this question we calculate the gravitational binding energy of a cloud with radius of ~ 80 -100 pc (\sim the maximum observed distances between

Table 3. Results from the statistical analysis for the distributions of the physical conditions and chemical abundances in the ISM across the INTEGRAL FOV of Mrk 178.

ISM property	Statistical properties				Sign.(%) ^e
	μ_{weighted}^a	$\sigma_{\text{weighted}}^b$	μ_{Gaussian}^c	$\sigma_{\text{Gaussian}}^d$	
$\log([\text{OII}]/[\text{OIII}])$	-0.56	0.33	—	—	< 10
$n([\text{SII}]) \text{ (cm}^{-3}\text{)}$	110	95	—	—	< 10
$T([\text{OIII}]) \text{ (K)}$	16770	760	17885	2200	26
$12+\log(\text{O}/\text{H})$ (direct method)	7.72	0.13	7.69	0.12	80
$12+\log(\text{O}/\text{H})$ (N2 method)	7.84	0.16	7.87	0.16	43
$\log(\text{N}/\text{O})$ (direct method)	-1.40	0.17	-1.34	0.16	37
$\log(\text{N}/\text{O})$ (N2O2 method)	-1.42	0.19	-1.38	0.17	75

(a) error-weighted mean; (b) square root of the weighted sample variance associated with the corresponding weighted mean; (c) mean of the Gaussian distribution; (d) standard deviation of the Gaussian distribution; (e) significance level of the null hypothesis in the Lilliefors test. We assume that the distribution of a certain property can be represented by a Gaussian fit if the null hypothesis is not rejected (i.e. Sig. > 10%)

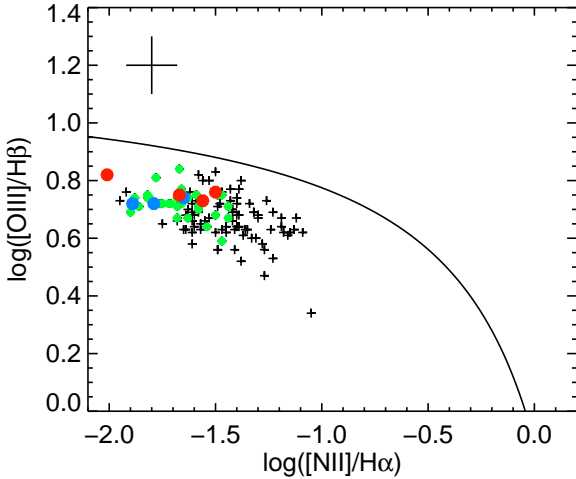


Figure 10. $\log([\text{OIII}]\lambda 5007/\text{H}\beta)$ vs. $\log([\text{NII}]\lambda 6584/\text{H}\alpha)$. Green circles show nebular HII -emitting spaxels with no WR features, blue circles show the spaxels with blue WR bump (knot A in Fig. 5) and red circles the spaxels showing both the blue and red WR bumps (knots B and C in Fig. 5). The remaining spaxels are indicated with cross-symbols. Typical uncertainties on the line ratios are indicated by the cross on the top-left of the panel. The plotted measurements are corrected for reddening. The black solid curve is the theoretical maximum starburst model from Kewley et al. (2001), devised to isolate objects whose emission line ratios can be accounted for by the photoionization by massive stars (below and to the left of the curve) from those where some other source of ionization is required.

the WR stars and nebular HeII across the FOV sampled here; see the map of $\text{HeII}\lambda 4686$ in Fig. 5) and assuming a hydrogen density of $\sim 100 \text{ cm}^{-3}$. From this calculation we obtain that the en-

ergy required to excavate a hole of this size is $\sim 10^{51-52}$ erg. We checked that this number is of the order of the predicted mechanical energy injected into the ISM due to massive star winds taking into account the number of WR stars derived in section 3.1. These predictions are based on evolutionary synthesis models by Mollá, García-Vargas, & Bressan (2009) for an HII region with Salpeter IMF and SMC-metallicity. Also, it is worthwhile remembering that WR stars with high temperatures ($T_{\star} \gtrsim 40 \text{ kK}$) and weak winds are expected to be capable of producing HeII ionizing photons (e.g., Crowther & Hadfield 2006). WC stars in knots B and C within Mrk 178 certainly appear to satisfy both criteria, although not exactly where nebular $\text{HeII}\lambda 4686$ is seen, as discussed above. We should bear in mind that the precise geometry of the ionized ISM distribution in the close environment of these knots clearly plays a role. If WR stars from knot A were responsible for the nebular HeII emission in this knot, some of the WN stars would need to be early-types, which cannot be ruled out from our WR template fits analysis. Additionally, according to the spectral classification scheme indicated in Fig. 10, for most positions in Mrk 178 our emission line ratios fall in the general locus of star-forming objects suggesting that hot massive stars are the dominant ionizing source within our FOV.

3.3 Aperture effects

Brinchmann, Kunth, & Durret (2008) presented a study of WR galaxies based on spectra from SDSS DR6 and found Mrk 178 to have the strongest WR features relative to $\text{H}\beta$ of any galaxy in the sample (see their Figs.18 and 19) which is intriguing if one considers the low metallicity of Mrk 178. This curious behaviour was possibly attributed to the fact that, due to the proximity of Mrk 178 (one of the closest systems in the sample of

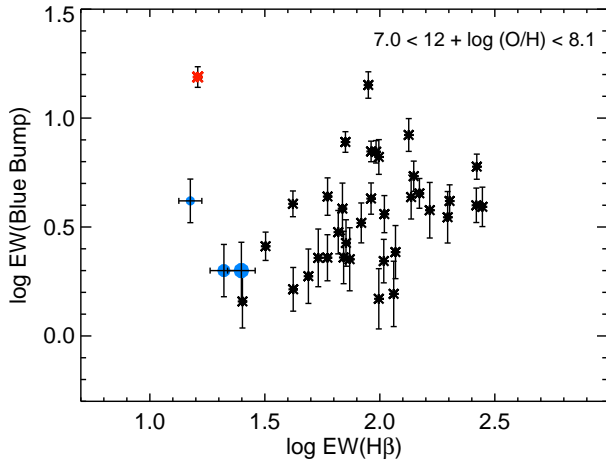


Figure 11. EW(blue WR bump) vs EW($H\beta$). Asterisks show values obtained from SDSS DR7 for metal-poor WR galaxies [$7.0 \lesssim 12 + \log(O/H) \lesssim 8.1$]; the red asterisk represents Mrk 178. The three blue circles, from the smallest to the biggest one, represent the 5, 7 and 10 arcsec-diameter apertures from our data centered at knot B. For the majority of the points the uncertainty of $\log[EW(H\beta)]$ is of the order of the symbol size.

Brinchmann, Kunth, & Durret 2008), the SDSS fiber could have by chance hit one single/few luminous WR stars while the $H\beta$ flux is more extended. Actually looking at the $H\alpha$ map in Fig. 5 we see that the Balmer line emission is more extended and its peak is offset from the WR emission which also indicates propagation of star formation; where the WR stars are now, the O stars are no longer. Here we take advantage of the IFS to investigate how the observations of WR signatures are affected by aperture effects.

In Fig. 11 we show EW(WR blue bump) vs EW($H\beta$) obtained from SDSS DR7 spectra of low metallicity [$7.0 \lesssim 12 + \log(O/H) \lesssim 8.1$] WR galaxies and we find the same discrepancy reported by Brinchmann, Kunth, & Durret (2008), i.e. the most deviant point (red asterisk) in Fig. 11 belongs to the galaxy Mrk 178. Using our IFU data we construct one-dimensional spectra by combining spaxels within circular apertures of increasing diameter (the center of all apertures coincides with our WR Knot B which is approximately the center of the Mrk 178 SDSS fiber). The measurements derived from these spectra are blue circles in Fig. 11 which show that Mrk 178 is brought closer to the bulk of metal-poor systems when the aperture size increases confirming that the offset between Mrk 178 and the rest of the objects as viewed by SDSS is not real and caused by aperture effect instead. We also checked that for apertures with diameter larger than ~ 10 arcsec we no longer detect the WR bump. This likely happens because the underlying stellar absorption masks the WR stellar signatures more easily if the apertures are too large. In metal-poor systems there is an enhancement of this effect since WR stars are expected to have weaker lines than in more metal rich environments (Conti, Garmany, & Massey 1989; Crowther & Hadfield 2006). In addition, after correcting the EW(WR blue bump) by the physical area of the SDSS aperture for each object in Fig. 11, we verified that the measurements of EW(WR blue bump) for all galaxies (not only Mrk 178) suffer from some degree of aperture effects (see also Pérez-Montero & Díaz 2007). All this can explain why sometimes WR features are not detected when they are expected to be present (see also James, Tsamis, & Barlow 2010).

4 SUMMARY AND CONCLUSIONS

We have presented here the first optical IFS study of the metal-poor WR galaxy Mrk 178. The proximity of Mrk 178 combined with the IFS technique allow us to locate and resolve star-forming knots hosting a few WR stars, and also to characterize the WR content. In addition we are able to probe the spatial correlation between massive stars and the properties of the surrounding ISM. In the following we list the main results derived from this work.

- We defined three WR knots from which two are identified for the first time here. The WR knot spectra reveal the presence of nitrogen-type and carbon-type WR stars in Mrk 178. By comparing the observed spectra of the WR knots with SMC and LMC template WR stars we estimate a lower limit for the number of WR stars ($\gtrsim 20$) in our Mrk 178 FOV that is already higher than that currently found in the literature (~ 2 -3 WR stars from Guseva, Izotov, & Thuan 2000). This is probably because IFS not only allows us to sample a larger area of the galaxy, but also offers a more powerful technique in searching for WR stars. As was demonstrated in Kehrig et al. (2008), using IFS one can find WR stars where they were not detected before because IFS, in comparison with long-slit spectroscopy, can increase the contrast of the WR bump emission against the galaxy continuum, thus minimizing the WR bump dilution.

- Our statistical analysis suggests that spatial variations in the gaseous electron temperature exist and that the scatter in T_e can be larger than that in O/H within the observed FOV. Thus, caution should be exercised when analysing integrated spectra of giant HII regions/HII galaxies which do not necessarily represent the “local” ISM properties around massive star clusters.

- The nebular chemical abundance in Mrk 178 is homogeneous over spatial scales of hundreds of parsecs. This result is in agreement with previous work on ionized gas in HII galaxies and favours the scheme, discussed by Tenorio-Tagle (1996), in which the most recent products of massive star nucleosynthesis remain unobservable optically on timescales longer than the lifetime of HII regions. The representative metallicity of Mrk 178 derived here is $12 + \log(O/H) = 7.72 \pm 0.01$ (error-weighted mean value of O/H and its corresponding statistical error).

- To probe the presence of small-scale (~ 20 pc, our resolution element size) localized chemical variations, we performed a close inspection of the chemical abundances for the WR knots from which we find a possible localized N and He enrichment, spatially correlated with WR knot C.

- The nebular HeII emission appears extended and is likely related to ionization from hot stellar continua. We interpret the spatial offset between WR stars and nebular HeII-emitting regions as an effect of the mechanical energy injected by WR star winds. This agrees with results by Shirazi & Brinchmann (2012) and Kehrig et al. (2008). Caution should be exercised when the precise geometry of the ionized ISM is not considered. Shock-ionization and X-ray binaries are unlikely to be significant ionizing mechanisms since Mrk 178 is not detected in X-rays.

- Brinchmann, Kunth, & Durret (2008) report an unusual (too high) $L(\text{WR bump})/L(H\beta)$ ratio for Mrk 178 derived from its SDSS spectrum. The authors question this assuming that aperture effect can be an explanation. This is confirmed in this work with IFS. We

also demonstrate that using too large an aperture, the chance of detecting WR features decreases. This result indicates that WR galaxy samples/catalogues constructed on single fiber/long-slit spectrum basis may be biased in the sense that WR signatures can escape detection depending on the distance of the object and on the aperture size.

This paper shows the need to identify good targets, such as Mrk 178, and the power of IFS for investigating issues related with aperture effects. In particular, we show the effect of distance and metallicity on the search for WR features, and the extent to which physical variations in the ISM properties can be detected. In addition, we believe that this work makes way for future research of low metallicity, close-by objects aiming to survey and characterize the WR population and to identify Hen nebulae through high-spatial resolution imaging and IFS.

ACKNOWLEDGEMENTS

We are very grateful to our referee Prof. Anthony Moffat for his fruitful comments and suggestions on the manuscript. This work has been partially funded by research projects AYA2007-67965-C03-02 and AYA2010-21887-C04-01 from the Spanish PNAYA and CSD2006-00070 1st Science with GTC of the MICINN. RGB acknowledges support from the Spanish Ministerio de Ciencia e Innovación through grant AYA2010-15081. FD acknowledges financial support from CNES.

The STARLIGHT project is supported by the Brazilian agencies CNPq, CAPES, and FAPESP. This paper uses the plotting package jmaplot developed by Jesús Maíz-Apellániz (available at <http://dae45.iaa.csic.es:8080~jmaiz/software>). This research made use of the NASA/IPAC Extragalactic Database (NED) which is operated by the Jet Propulsion Laboratory, California Institute of Technology, under contract with the National Aeronautics and Space Administration.

This paper makes use of the Sloan Digital Sky Survey data. Funding for SDSS and SDSS-II has been provided by the Alfred P. Sloan Foundation, the Participating Institutions, the National Science Foundation, the US Department of Energy, the National Aeronautics and Space Administration, the Japanese Monbukagakusho, the Max Planck Society, and the Higher Education Funding Council for England. The SDSS web site is <http://www.sdss.org/>. SDSS is managed by the Astrophysical Research Consortium for the Participating Institutions. The Participating Institutions are the American Museum of Natural History, Astrophysical Institute Potsdam, University of Basel, University of Cambridge, Case Western Reserve University, University of Chicago, Drexel University, Fermilab, the Institute for Advanced Study, the Japan Participation Group, Johns Hopkins University, the Joint Institute for Nuclear Astrophysics, the Kavli Institute for Particle Astrophysics and Cosmology, the Korean Scientist Group, the Chinese Academy of Sciences (LAMOST), Los Alamos National Laboratory, the Max-Planck-Institute for Astronomy (MPIA), the Max-Planck-Institute for Astrophysics (MPA), New Mexico State University, Ohio State University, University of Pittsburgh, University of Portsmouth, Princeton University, the United States Naval Observatory, and the University of Washington.

REFERENCES

- Asplund M., Grevesse N., Sauval A. J., Scott P., 2009, *ARA&A*, 47, 481
- Bingham R. G., Gellatly D. W., Jenkins C. R., Worswick S. P., 1994, *SPIE*, 2198, 56
- Brinchmann J., Kunth D., Durret F., 2008, *A&A*, 485, 657
- Bruzual G., Charlot S., 2003, *MNRAS*, 344, 1000
- Buckalew B. A., Kobulnicky H. A., Dufour R. J., 2005, *ApJS*, 157, 30
- Cairós L. M., Caon N., Papaderos P., Kehrig C., Weilbacher P., Roth M. M., Zurita C., 2009a, *ApJ*, 707, 1676
- Cairós L. M., Caon N., Zurita C., Kehrig C., Weilbacher P., Roth M., 2009b, *A&A*, 507, 1291
- Cairós L. M., Caon N., Zurita C., Kehrig C., Roth M., Weilbacher P., 2010, *A&A*, 520, A90
- Campos-Aguilar A., Moles M., Masegosa J., 1993, *AJ*, 106, 1784
- Cardelli J. A., Clayton G. C., Mathis J. S., 1989, *ApJ*, 345, 245
- Chabrier G., 2003, *PASP*, 115, 763
- Cid Fernandes R., Gu Q., Melnick J., Terlevich E., Terlevich R., Kunth D., Rodrigues Lacerda R., Joguet B., 2004, *MNRAS*, 355, 273
- Cid Fernandes R., Mateus A., Sodré L., Stasińska G., Gomes J. M., 2005, *MNRAS*, 358, 363
- Conti P. S., Garmany C. D., Massey P., 1989, *ApJ*, 341, 113
- Crowther P. A., Smith L. J., Hillier D. J., Schmutz W., 1995, *A&A*, 293, 427
- Crowther P. A., De Marco O., Barlow M. J., 1998, *MNRAS*, 296, 367
- Crowther P. A., Drissen L., Abbott J. B., Royer P., Smartt, S. J., 2003, *A&A* 404, 483
- Crowther P. A., Hadfield L. J., 2006, *A&A*, 449, 711
- Crowther P. A., Carpano S., Hadfield L. J., Pollock A. M. T., 2007, *A&A*, 469, L31
- Crowther P. A., 2007, *ARA&A*, 45, 177
- de Mello D. F., Schaerer D., Heldmann J., Leitherer C., 1998, *ApJ*, 507, 199
- DeVaucouleurs G., De Vaucouleurs A., Corwin H. G., Jr Buta R. J., Paturel G., Fouque P., 1991, *Third Reference Catalogue of Bright Galaxies*, Version 3.9
- Drissen L., Moffat A. F. J., Walborn, N. R., Shara M. M., 1995, *AJ*, 110, 2235
- Eldridge J. J., Stanway E. R., 2009, *MNRAS*, 400, 1019
- Esteban C., Vilchez J. M., 1992, *ApJ*, 390, 536
- Fernández-Martín A., Martín-Gordón D., Vilchez J. M., Pérez Montero E., Riera A., Sánchez S. F., 2012, *A&A*, 541, A119
- Foellmi C., Moffat A. F. J., Guerrero M. A., 2003, *MNRAS*, 338, 360
- Foellmi C., Moffat A. F. J., Guerrero M. A., 2003, *MNRAS*, 338, 1025
- García-Benito R., et al., 2010, *MNRAS*, 408, 2234
- García-Benito R., Pérez-Montero E., 2012, *MNRAS*, 423, 406
- Garnett D. R., Kennicutt R. C., Jr., Chu Y.-H., Skillman E. D., 1991, *ApJ*, 373, 458
- Gil de Paz A., Madore B. F., Pevunova O., 2003, *ApJS*, 147, 29
- Gil de Paz A., Madore B. F., 2005, *ApJS*, 156, 345
- Gonzalez-Delgado R. M., et al., 1994, *ApJ*, 437, 239
- Gonzalez-Delgado R. M., et al., 1996, *ApJ*, 473, 1125
- Gonzalez-Riestra R., Rego M., Zamorano J., 1988, *A&A*, 202, 27
- Guseva N. G., Izotov Y. I., Thuan T. X., 2000, *ApJ*, 531, 776
- Hadfield L. J., Crowther P. A., 2006, *MNRAS*, 368, 1822
- Izotov Y. I., Thuan T. X., Lipovetsky V. A., 1994, *ApJ*, 435, 647
- Izotov Y. I., Thuan T. X., Stasińska G., 2007, *ApJ*, 662, 15

- Izotov Y. I., Guseva N. G., Fricke K. J., Papaderos P., 2009, *A&A*, 503, 61
- James B. L., Tsamis Y. G., Barlow M. J., 2010, *MNRAS*, 401, 759
- Karachentsev I. D., et al., 2003, *A&A*, 398, 467
- Kehrig C., Telles E., Cuisinier F., 2004, *AJ*, 128, 1141
- Kehrig C., Vílchez J. M., Telles E., Cuisinier F., Pérez-Montero E., 2006, *A&A*, 457, 477
- Kehrig C., Vílchez J. M., Sánchez S. F., Telles E., Pérez-Montero E., Martín-Gordón D., 2008, *A&A*, 477, 813
- Kehrig C., et al., 2011, *A&A*, 526, A128
- Kewley L. J., Dopita M. A., Sutherland R. S., Heisler C. A., Trevena J., 2001, *ApJ*, 556, 121
- Kingsburgh R. L., Barlow M. J., Storey P. J., 1995, *A&A*, 295, 75
- Kingsburgh R. L., Barlow M. J., 1995, *A&A*, 295, 171
- Kobulnicky H. A., Skillman E. D., 1996, *ApJ*, 471, 211
- Kobulnicky H. A., Skillman E. D., 1997, *ApJ*, 489, 636
- Kobulnicky H. A., Skillman E. D., Roy J.-R., Walsh J. R., Rosa M. R., 1997, *ApJ*, 477, 679
- Kunth D., Sargent W. L. W., 1981, *A&A*, 101, L5
- Le Borgne J.-F., Bruzual G., Pelló R., Lançon A., Rocca-Volmerange B., Sanahuja B., Schaerer D., Soubiran C., Vílchez-Gómez R., 2003, *A&A*, 402, 433
- Lebouteiller V., Kunth D., Thuan T. X., Désert J. M., 2009, *A&A*, 494, 915
- Lee H., Skillman E. D., 2004, *ApJ*, 614, 698
- Lee J. C., et al., 2009, *ApJ*, 706, 599
- Legrand F., Kunth D., Roy J.-R., Mas-Hesse J. M., Walsh J. R., 1997, *A&A*, 326, L17
- Leitherer C., Schaerer D., Goldader J. D., Delgado R. M. G., Robert C., Kune D. F., de Mello D. F., Devost D., Heckman T. M., 1999, *ApJS*, 123, 3
- Lilliefors, H. W., 1967, *J. Amer. Statistical Assoc.*, 62, 399
- López-Sánchez Á. R., Mesa-Delgado A., López-Martín L., Esteban C., 2011, *MNRAS*, 411, 2076
- Maeder A., 1992, *A&A*, 264, 105
- Markarian B. E., 1969, *Afz*, 5, 581
- Mateus A., Sodré L., Cid Fernandes R., Stasińska G., Schoenell W., Gomes J. M., 2006, *MNRAS*, 370, 721
- Melnick J., Terlevich R., Eggleton P. P., 1985, *MNRAS*, 216, 255
- Meynet G., Maeder A., 2005, *A&A*, 429, 581
- Modjaz M., et al., 2008, *AJ*, 135, 1136
- Moffat, A. F. J., Seggewiss W., Shara, M. M. 1985, *ApJ* 295, 109
- Moll S. L., Mengel S., de Grijs R., Smith L. J., Crowther P. A., 2007, *MNRAS*, 382, 1877
- Mollá M., García-Vargas M. L., Bressan A., 2009, *MNRAS*, 398, 451
- Monreal-Ibero A., Walsh J. R., Vílchez J. M., 2012, *A&A*, 544, A60
- Munoz-Tunon C., Tenorio-Tagle G., Castaneda H. O., Terlevich R., 1996, *AJ*, 112, 1636
- Neugent K. F., Massey P., 2011, *ApJ*, 733, 123
- Olive K. A., Skillman E. D., 2004, *ApJ*, 617, 29
- Pagel B. E. J., Terlevich R. J., Melnick J., 1986, *PASP*, 98, 1005
- Papaderos P., Östlin G., 2012, *A&A*, 537, A126
- Pérez-Montero E., Díaz A. I., 2003, *MNRAS*, 346, 105
- Pérez-Montero E., Díaz A. I., 2005, *MNRAS*, 361, 1063
- Pérez-Montero E., Díaz Á. I., 2007, *MNRAS*, 377, 1195
- Pérez-Montero E., Contini T., 2009, *MNRAS*, 398, 949
- Pérez-Montero E., García-Benito R., Díaz A. I., Pérez E., Kehrig C., 2009, *A&A*, 497, 53
- Pérez-Montero E., García-Benito R., Hägele G. F., Díaz Á. I., 2010, *MNRAS*, 404, 2037
- Pérez-Montero E., et al., 2011, *A&A*, 532, A141
- Popescu C. C., Hopp U., 2000, *A&AS*, 142, 247
- Recchi S., Matteucci F., D'Ercole A., Tosi M., 2003, *Ap&SS*, 284, 623
- Recchi S., Hensler G., 2013, *arXiv*, arXiv:1301.0812
- Roy J.-R., Kunth D., 1995, *A&A*, 294, 432
- Russell S. C., Dopita M. A., 1990, *ApJS*, 74, 93
- Sandin C., Becker T., Roth M. M., Gerssen J., Monreal-Ibero A., Böhm P., Weilbacher P., 2010, *A&A*, 515, A35
- Schaerer D., Contini T., Pindao M., 1999, *A&AS*, 136, 35
- Schlegel D. J., Finkbeiner D. P., Davis M., 1998, *ApJ*, 500, 525
- Schmutz W., Leitherer C., Gruenwald R., 1992, *PASP*, 104, 1164
- Schnurr O., Moffat A. F. J., St-Louis N., Morrell N. I., Guerrero M. A., 2008, *MNRAS*, 389, 806
- Shaw R. A., Dufour R. J., 1994, *ASPC*, 61, 327
- Shirazi M., Brinchmann J., 2012, *MNRAS*, 421, 1043
- Sidoli F., Smith L. J., Crowther P. A., 2006, *MNRAS*, 370, 799
- Smith L. F., 1973, *IAUS*, 49, 15
- Smith R. C., Kirshner R. P., Blair W. P., Long K. S., Winkler P. F., 1993, *ApJ*, 407, 564
- Smith L. F., Shara M. M., Moffat A. F. J., 1996, *MNRAS*, 281, 163
- Stevens I. R., Strickland D. K., 1998, *MNRAS*, 294, 523
- Stock D. J., Barlow M. J., 2010, *MNRAS*, 409, 1429
- Storey P. J., Hummer D. G., 1995, *MNRAS*, 272, 41
- Tenorio-Tagle G., 1996, *AJ*, 111, 1641
- van Zee L., Haynes M. P., 2006, *ApJ*, 636, 214 (HII regions in dwarf irregular galaxies)
- Vílchez J. M., Iglesias-Páramo J., 1998, *ApJ*, 508, 248
- York D. G., et al., 2000, *AJ*, 120, 1579
- Westera P., Cuisinier F., Telles E., Kehrig C., 2004, *A&A*, 423, 133
- Westera P., Cuisinier F., Curty D., Buser R., 2012, *MNRAS*, 421, 398
- Woosley S. E., Bloom J. S., 2006, *ARA&A*, 44, 507